Materials Transactions, Vol. 67, No. 4 (2026) pp. 535 to 542

Integrated Computational and Experimental Study on Rapid Heating and Cooling Conditions in Powder-Bed Fusion of Al-Si Hypoeutectic Alloys

Masayuki Okugawa[1,2,*], Yuya Furushiro[1], Seori Motoyama[1], Yuheng Liu[1], Takayoshi Nakano[1,2] and Yuichiro Koizumi[1,2,*]

[1]*Graduate School of Engineering, The University of Osaka, Suita 565-0871, Japan*
[2]*Anisotropic Design & Additive Manufacturing Research Center, The University of Osaka, Suita 565-0871, Japan*

Al alloy parts fabricated by powder-bed fusion (PBF) have garnered significant attention, and inoculant rare-earth elements are typically introduced to enhance their mechanical properties. However, extracting rare-earth elements raises powder costs and mining poses environmental risks. Therefore, a novel grain refinement method for the PBF process that does not rely on inoculation is needed. We previously proposed that the intrinsic heterogeneous nucleation caused by rapid heating during the PBF process is key to a novel grain refinement strategy. It is essential to understand the relationships between laser irradiation parameters, melting and solidification conditions, and the resulting microstructure to provide guidelines for microstructure control in the PBF process. In this study, we investigated melting and solidification conditions in the PBF process of Al-Si hypoeutectic alloy by computational thermal-fluid dynamics simulations. It was found that the heating rates in the PBF process are around 10^8 K/s and are 10 times higher than the cooling rates, and these rapid heating and cooling conditions are suggested to cause the intrinsic heterogeneous nucleation unique to the PBF of the Al-Si hypoeutectic alloy. Furthermore, the melting and solidification conditions vary significantly within the melt pool, and the experimental microstructural inhomogeneity at the melt pool boundary can be explained based on the distribution of melting and solidification conditions. In addition to the rapid solidification unique to the PBF process, the focus on rapid heating paves the way for a wider range of microstructure control. [doi:10.2320/matertrans.MT-M2025132]

(Received October 1, 2025; Accepted December 20, 2025; Published March 25, 2026)

Keywords: *additive manufacturing, laser powder-bed fusion, Al-Si hypoeutectic alloy, computational thermal-fluid dynamics*

1. Introduction

Recently, additive manufacturing (AM) technology has received attention due to its ability to produce complex shapes [1–4]. Application of AM to aluminum (Al) alloys is expected to reduce weight while maintaining strength, particularly in the fields of aerospace and automotive [5–11]. Among the AM processes, powder-bed fusion (PBF) type AM has emerged as a preferred technique for metal AM [12–18]. In the PBF, inoculant elements such as scandium are introduced to form heterogeneous nucleation sites, thereby enhancing the mechanical properties of Al alloy components. However, the extraction of rare-earth elements increases powder costs [19], and mining poses environmental risks, such as soil contamination [20]. Therefore, a novel grain refinement method for the PBF process that does not require inoculant elements is necessary.

We are focusing on the anomalous microstructure observed in PBF-type AM of Al-Si hypoeutectic alloys to develop a grain refinement process. The microstructure formation in Al-Si hypoeutectic alloys [21] differs from that predicted by the conventional columnar-to-equiaxed transition criteria proposed by Hunt [22]: equiaxed grains form at the melt pool boundary, while columnar crystals form in the central region. In a previous study, we suggested that rapid heating during melting significantly affects microstructure formation in the Al-Si hypoeutectic alloy, where there are large differences in the melting points of the constituent phases [23]. We demonstrated through multi-phase field (MPF) simulations that inhomogeneous melting occurs under the rapid heating conditions assumed for the LPBF process, and the remaining Si particles act as heterogeneous nucleation sites during subsequent resolidification. Additionally, MPF simulations with optimized initial solidification, remelting, and recrystallization conditions predicted the formation of finer equiaxed microstructures around 12.3 μm [24].

Most of the studies of microstructural formation in the PBF-type AM process focus on the unique rapid solidification conditions. On the other hand, we suggested that the rapid heating conditions are also crucial for microstructure formation for eutectic alloys with significant differences in melting points, such as Al-Si alloys. Thus, it is necessary to reveal the relationship between laser irradiation conditions, melting and solidification conditions, and the formed microstructure for the guideline of microstructure control in the PBF process. However, no studies have systematically investigated melting conditions, although there are extensive studies on solidification conditions.

In the present study, we investigated rapid heating and cooling conditions in the PBF process using computational thermal fluid dynamics (CtFD) calculations, which were validated by experiments. The CtFD simulations were performed under various laser power and scanning speed conditions, and the melting and solidification conditions were evaluated. Furthermore, we compare the microstructures formed in the Al-Si build part and predicted by phase-field simulations to provide a guideline for microstructure control that incorporates these melting conditions.

2. Experimental Procedures and Simulation Methods

The Al-10 mass% Si (Al-10Si) alloy was prepared by melting pure Al and Si in an alumina crucible under a 99.999% pure Ar atmosphere. The bulk was laser irradiated using a laser PBF-type AM machine (EOS M290). In the

*Corresponding authors, E-mail: okugawa@mat.eng.osaka-u.ac.jp, ykoizumi@mat.eng.osaka-u.ac.jp

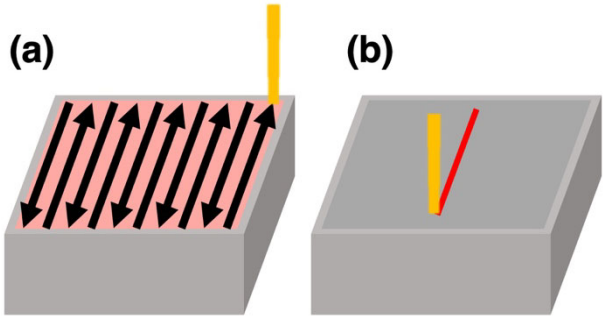

Fig. 1 Schematic illustrations of the laser irradiation experiment. (a) Multi-track scanning for microstructure homogenization and (b) single-track scanning. (online color)

laser irradiation experiment, the as-cast microstructure is coarse relative to the melt pool size and would affect its melting and solidification behavior. Thus, the region for single-track irradiation experiments was pre-scanned under the conditions with laser power $P = 360\,\mathrm{W}$ and scanning speed $V = 800\,\mathrm{mm/s}$, as schematically shown in Fig. 1(a). Then, laser irradiations were performed to form a single bead with a scanning distance of 1000 µm under various beam irradiation conditions shown in Table 1 (Fig. 1(b)). The cross-section of the formed melt pool was observed using an optical microscope (Olympus DSX1000) and a field emission scanning electron microscope (FE-SEM, JEOL JSM6500).

The CtFD simulations were performed using the same laser irradiation conditions as those in the experiments. The CtFD simulations were performed using a general 3D thermal-fluid analysis software (Flow Science FLOW-3D®). The laser beam was linearly scanned for 5000 µm to investigate the temporal evolution of the temperature distribution. The simulation is composed of two computational domains: a 7000 µm × 400 µm × 1200 µm domain with a mesh size of 10 × 10 × 10 µm for the laser-irradiated region and a 9720 µm × 3120 µm × 1200 µm domain with a mesh size of 50 × 50 × 50 µm for the other area. Table 2 shows the thermodynamic properties used for the simulation. The initial substrate temperature and the atmospheric pressure were set to 300 K and 1.013×10^5 Pa, respectively. The energy absorption rate η was calculated assuming multiple reflections using the Fresnel equation:

Table 1 Irradiation conditions and corresponding line energies.

Line energy, $E_{line} = P/V$ (J/mm)		Scan speed, V (mm/s)		
		800	1000	1200
Beam Power, P (W)	360	0.45	0.36	0.3
	300	0.375	0.3	0.25
	240	0.3	0.24	0.2

Table 2 Thermophysical properties used in CtFD simulations.

Thermophysical properties		Value	Sources
Density (298.15K)	kg/m³	2670	[25]
Viscosity (1683.68K)	kg/(m s)	1.38×10^{-3}	[26]
Specific heat (298.15K)	J/(kg K)	546.6	
Thermal conductivity (298.15K)	W/(m K)	116	
Liquidus temperature	K	867	[25]
Solidus temperature	K	850	
Latent heat of fusion	J/kg	4.23×10^5	
Surface tension (1683.68K)	kg/s²	1000 - 0.152T	[27]
Latent heat of vaporization	J/kg	1.07×10^7	[25]
Saturation temperature (1atm)	K	2743	

$$\eta = 1 - \frac{1}{2}\left\{\frac{1+(1-\varepsilon\cos\theta)^2}{1+(1+\varepsilon\cos\theta)^2} + \frac{\varepsilon^2 - 2\varepsilon\cos\theta + 2\cos^2\theta}{\varepsilon^2 + 2\varepsilon\cos\theta + 2\cos^2\theta}\right\} \quad (1)$$

where ε and θ are the Fresnel coefficient and the incident angle of the laser, respectively. The ε was used as a fitting parameter and adjusted to reproduce the experimental melt pool depth. The cooling rate, heating rate, temperature gradient, and solid-liquid interfacial velocity during the melting and solidification process were evaluated from the change in the temperature distributions.

To compare the simulation-predicted and actual microstructures, Al-10Si parts with dimensions of $10 \times 10 \times 10$ mm were fabricated using a PBF-type AM machine (EOS M 290) in an Ar atmosphere with an oxygen content below 0.1%. The gas-atomized Al-10Si spherical powders (Toyo Aluminium) were used for the fabrication. The beam power P, scanning speed V, hatch spacing, and layer thickness were 360 W, 800 mm/s, 100 µm, and 40 µm, respectively. The laser scanning direction was only in the x-directions. The cross-section of the fabricated specimen was analyzed by the SEM equipped with an electron backscatter diffraction (EBSD) detector.

3. Results and Discussions

3.1 Transition from thermal conduction melting to keyhole melting occurs in a single-track formation

Figure 2(a) shows an optical microscope image of a cross-section perpendicular to the scanning direction of the irradiated laser beam. It was found that the melt pool shape largely depends on the line energies of the laser irradiation: melt pools formed by laser irradiation under conditions with line energies of 0.3 J/mm or less were significantly smaller than melt pools with higher line energies. Figure 2(b) shows the relation between line energy and melt pool depth, and tendency changes at the line energy of 0.3 J/mm. It has been reported that the shape of the melt pool changes continuously with the amount of line energy in stainless steels [28] and Ni-based superalloy [29, 30]. On the other hand, the melt pool depth changed discontinuously with the amount of input energy for the Al-10Si alloy.

The CtFD laser irradiation simulations for single track formation were performed to clarify the behavior within the sample during melting and solidification. Figure 3(a1) shows a longitudinal cross-sectional snapshot of the melt pool formed under $P = 360$ W and $V = 1200$ mm/s conditions, and the depth of the melt pool transitions discontinuously during the laser irradiation process. The drastic change in size of the melt pool, which was observed experimentally, also occurred in the simulation. This suggests that the transition occurs based on physics. To obtain a deeper understanding of the transition, the single-track simulations with various Fresnel coefficients ε. Figures 3(a2) and 3(a3) show the cross-sections of the melted region parallel to the scanning direction. The transition in melt pool depth was also observed, and the coordination of the transition was found to depend on the Fresnel coefficient: The time until the transition begins decreases with increasing Fresnel coefficient. Thus, input heat is supposed to be related to the

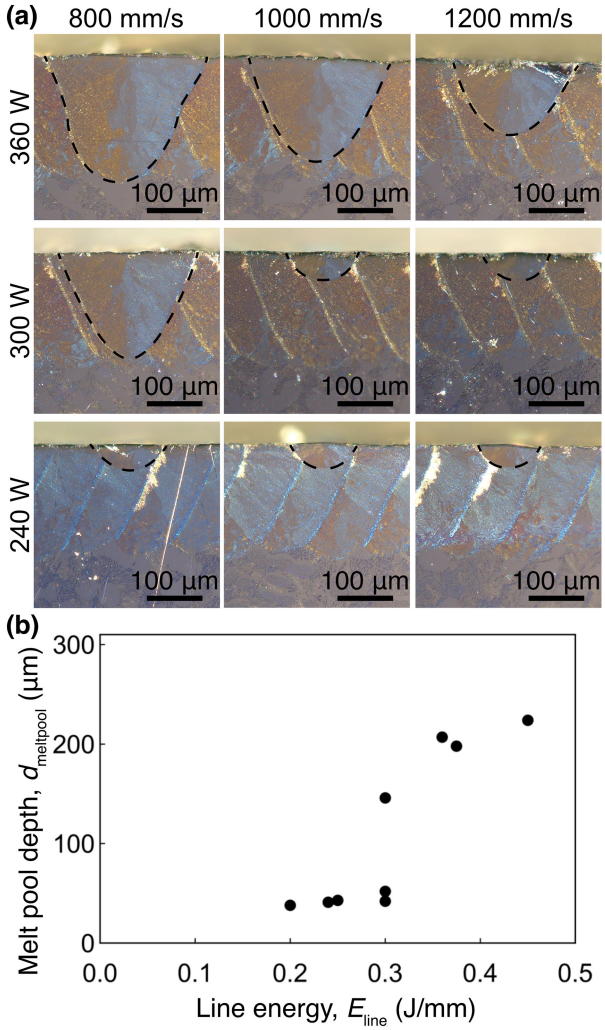

Fig. 2 (a) Optical microscope images of the cross section of the melt pool formed by various scanning speeds and laser beam power with Al-10Si casting alloy, and (b) melt pool depths. (online color)

transition, and we investigated the temperature changes of the regions near the melt indicated by white square in Fig. 3(b). Figure 3(c1)–(c3) shows the average temperature just before melting at each place in the direction parallel to the laser scanning direction. The dashed black line indicates the transition point of the melt pool formation behavior. It was found that there is a threshold temperature, and a heat accumulation temperature of approximately 550 K is considered to cause a transition from heat conduction-type melt pool formation to keyhole-type melt pool formation.

Drastic changes in melt pool formation behavior with irradiation conditions have also been observed in pure copper [31], which has a high thermal conductivity of approximately 390 W/(m K). Al-10Si has a thermal conductivity of approximately 116 W/(m K) at 867 K, which is about five times greater than that of 304 stainless steel. Thus, the transition is caused by the rapid diffusion of absorbed heat owing to the high thermal conductivities of both Al-10Si and pure copper. In recent years, the PBF process has enabled us to control crystal orientation by controlling the overlapping of melt pools through laser scanning strategies [15], and understanding the factors that determine the shape of the melt pool formed by a single laser scan is crucial. Therefore, the

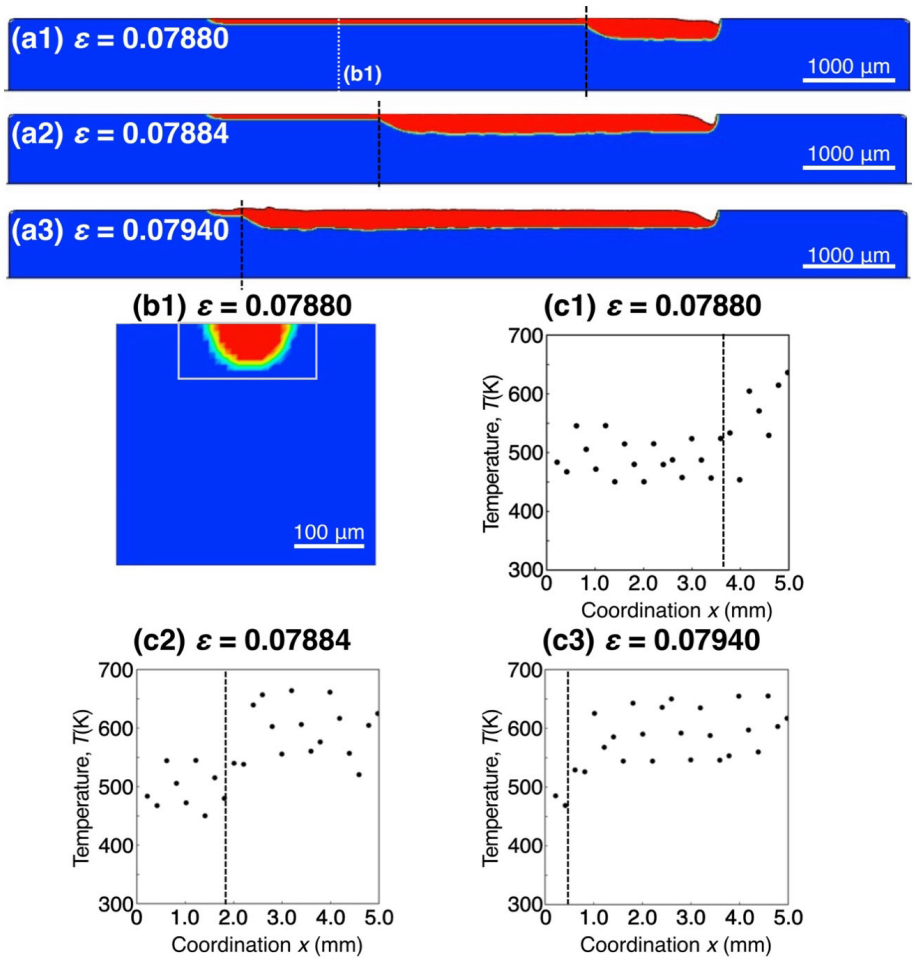

Fig. 3 (a1)–(a3) Snapshots of the cross-section of the melt pool formed by scanning laser beam under different Fresnel coefficients, ε. Beam power and scanning speed are $P = 300$ W and $V = 1200$ mm/s, respectively. (b1)–(b3) Temperature just before melting at each position in the direction parallel to the laser scanning for the same Fresnel coefficients. The dashed lines indicate the positions of the transition in the depth of the melt pool. (online color)

melt pool shape transition phenomenon identified in this study is considered to be one guideline for microstructure control.

3.2 Relationship between laser irradiation conditions and melting/solidification conditions

The temperature gradient G at the solid-liquid interface and the interface velocity R during melting and solidification were evaluated from the temperature distributions obtained through the CtFD simulations. Figures 4(a) and 4(b) show cross-sections and the G–R plot colored by the time each region melted and solidified. The P and V are 360 W and 800 mm/s, respectively. The temperature gradient G at the solid-liquid interface decreases as melting and solidification proceed. On the other hand, the liquid-solid interfacial velocity R decreases monotonically during melting and increases monotonically during solidification. The P and V are 360 W and 800 mm/s, respectively. The solidification occurred under the conditions around $G = 10^6$ K/m and $R = 10^1$ m/s. It is reported that the solidifications induced by electron/laser beam irradiations for the PBF processes occur under around $G = 10^6$ K/m and $V = 10^{-1}$ m/s in stainless steels [32] and under around $G = 10^7$ K/m and $V = 10^{-1}$ m/s in Ni-based superalloy [13]. Compared to these alloys, solidification in the Al-Si alloy is found to occur under 100 times larger interface velocity. It is supposed that the difference is caused by the lower heat capacity of 0.9 J/(g K) and the higher thermal conductivity of 116 W/(m K) of Al-10Si, which enables temperature change to occur quickly and heat to transfer easily, resulting in significantly higher cooling rates compared to other alloys.

Conversely, the melting occurred under $G = 10^7$ K/m and $R = 10^1$ m/s conditions. Melting occurs under a high solid-liquid interface velocity similar to that of solidification. On the other hand, the temperature gradient is ten times larger than that of the solidification. Figure 4(c) compares the heating and cooling rates at the same XZ coordinate on the cross-section (Fig. 4(a)). The heating rate is approximately ten times higher than the cooling rate in the same area because of the difference in temperature gradient. In the previous study, we demonstrated through multiphase-field (MPF) simulations that the Si particles in eutectic regions near the melt-pool boundary of a solidified Al-Si alloy remain after the remelting process [23]. According to the equilibrium phase diagram, heating from room temperature causes the eutectic microstructure to melt at the eutectic temperature via diffusion between the component phases. However, under the extremely rapid heating conditions in PBF processes, only

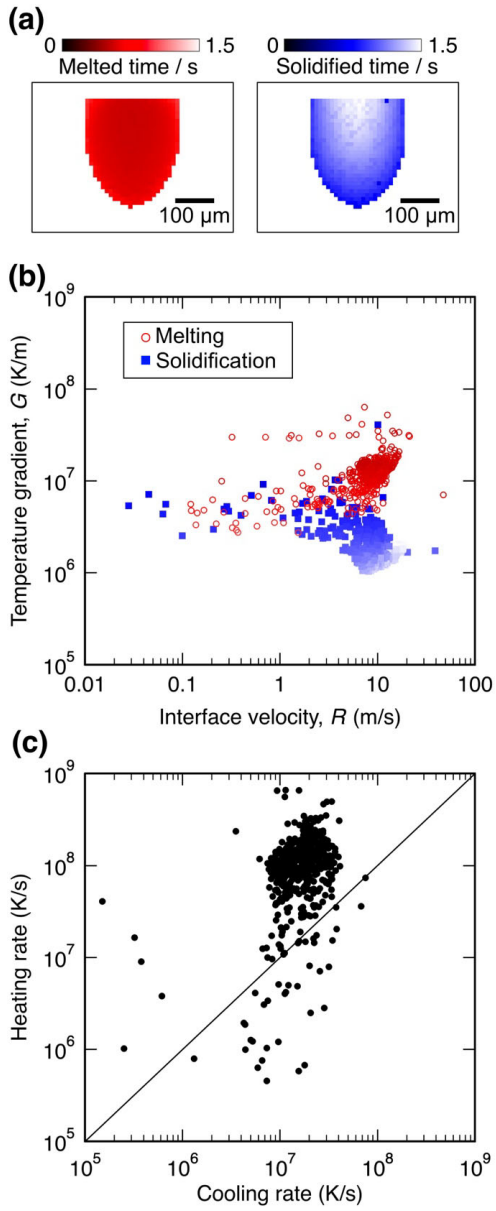

Fig. 4 (a) Melting and solidification conditions and (b) heating and cooling rate evaluated by the CtFD simulation. Beam power P and scan speed V are 360 W and 800 mm/s, respectively. (online color)

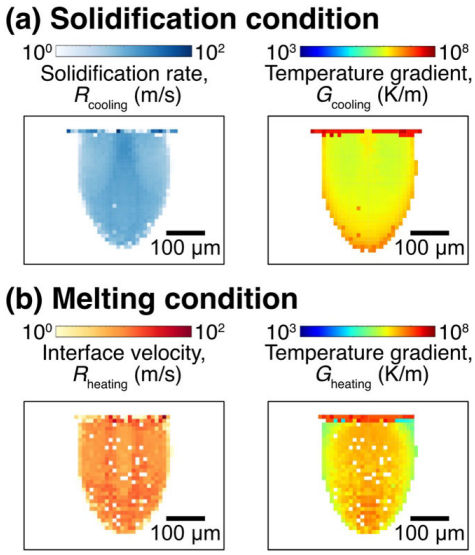

Fig. 5 CtFD simulated cross-sectional melt pools colored by (a) solidification conditions ($R_{cooling}$ and $G_{cooling}$) and (b) melting conditions ($R_{heating}$ and $G_{heating}$). Beam power P and scan speed V are 360 W and 800 mm/s, respectively. (online color)

the lower-melting-point α-Al phase melts due to the limited time for mixing. As a result, the Si phase, which has a melting point approximately 700 K higher than that of α-Al, remains and acts as a heterogeneous nucleation site for α-Al equiaxed crystalline grains in the subsequent resolidification process [23].

To obtain a guideline for controlling the microstructure based on the melting and solidification conditions, the distributions of G and R within the melt pool were investigated. Figure 5 shows cross-sectional melt pools colored by temperature gradient $G_{cooling}$ and solidification rate $R_{cooling}$ during the solidification process (Fig. 5(a)) and by temperature gradient $G_{heating}$ and solidification rate $R_{heating}$ during the melting process (Fig. 5(b)). The $G_{cooling}$ is highest in the regions near the fusion line (10^7 K/m) and decreases as the solid–liquid interface moves toward the center of the melt pool (10^6 K/m). The $R_{cooling}$ is lowest near the fusion line (1 m/s) and becomes higher as the interface approaches the center of the melt region (20 m/s). On the other hand, the $G_{heating}$ is lowest in the regions near the fusion line (10^6 K/m) and decreases as the solid–liquid interface moves toward the center of the melt pool (10^7 K/m). The $R_{heating}$ is lowest near the fusion line (1 m/s) and becomes higher as the interface approaches the center of the melt region (20 m/s). Comparing the solidification and melting conditions, R exhibits the same distribution trend within the melt pool, and is large in the central region. Conversely, G showed an opposite distribution. We proposed in the previous study [24] that initial solidification, remelting, and resolidification conditions influence the microstructure, resulting in various microstructure formations from fine equiaxed grain to columnar grain: the microstructure with the finest grains is expected to form under a high G and low R during initial solidification, a high heating rate during remelting, and a small G with a high R during resolidification. In contrast, columnar crystals grow epitaxially at the melt pool boundary under a small G and a high R during initial solidification, a low heating rate during remelting, and a large G and a low R during resolidification. Thus, the microstructure control can be achieved by controlling the overlap of the melt pool via a laser scanning strategy, such as adjusting the scanning pitch, to control local initial solidification, melting, and resolidification conditions based on the spatial distributions of solidification and melting conditions obtained in this study.

We investigated the relationship between the distributions of melting and solidification conditions and the laser irradiation conditions to obtain further guidelines for controlling the microstructure. Figure 6 shows the solidification and melting conditions within melt pools formed by laser irradiations with various beam powers P and scanning speeds V, respectively. Increasing the beam power and decreasing scanning speed, i.e., increasing line energy $E_{line} = P/V$, causes smaller melt pool formation. As a result, solidification occurs under lower $G_{cooling}$ and higher $R_{cooling}$

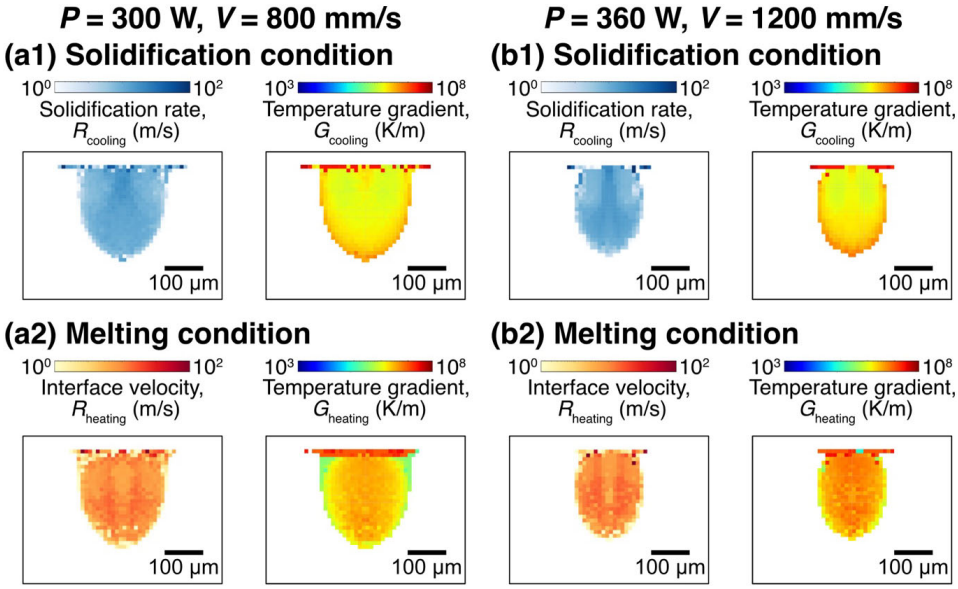

Fig. 6 CtFD simulated cross-sectional melt pools colored by (a1), (b1) solidification conditions ($R_{cooling}$ and $G_{cooling}$) and (a1), (b2) melting conditions ($R_{heating}$ and $G_{heating}$). Beam power P and scan speed V are (a1), (a2) 360 W and 800 mm/s and (b1), (b2) 360 W and 1200 mm/s. (online color)

conditions (Figs. 6(a1) and 6(a2)). On the other hand, increasing line energy E_{line} causes melting under higher $G_{heating}$, and $R_{heating}$ conditions (Figs. 6(b1) and 6(b2)). These results also suggest that increasing the line energy E_{line} increases the gap between the values of $G_{cooling}$, $R_{cooling}$, $G_{heating}$, and $R_{heating}$ inside the melt pool and at its boundary. It is expected that more advanced guidelines for microstructural control can be obtained by considering both solidification and melting conditions through laser irradiation conditions.

3.3 Comparison of the microstructures of the fabricated part and those predicted based on simulations

Figures 7(a1)–7(a3) show the SEM-EBSD grain map of the Al-10Si alloy fabricated by laser PBF. The laser power and scanning speed are 360 W and 800 mm/s, respectively. The melt pool boundary is indicated by the dotted lines. The formed microstructure differs significantly depending on the region within the melt pool. Equiaxed fine grains are formed on the right side of the melt pool boundary (Region A). In contrast, columnar crystals are formed on the left side of the melt pool boundary (Region B). This microstructural heterogeneity is attributed to differences in initial solidification, remelting, and resolidification conditions resulting from melt pool overlapping.

Figure 7(b) shows the schematic illustrations of the overlap of melt pools at regions A and B. Both regions are placed at melt pool boundaries; thus, the remelting and resolidification conditions are considered to be the same. Therefore, the heterogeneity in the microstructure is attributed to differences in the initial solidification condition. Based on the results of the CtFD simulations shown in Section 3.2, solidification occurs at the melt pool boundary under higher $G_{cooling}$ and lower $R_{cooling}$ conditions compared to the central part of a melt pool. In Region A, initial solidification occurs at the melt pool boundary, and remelting and recrystallization also occur at the boundary. Considering the distribution of solidification conditions within the melt pool, the initial solidification is suggested to occur under higher $G_{cooling}$ and lower $R_{cooling}$ conditions. PF simulations predict the formation of equiaxed grain structures under these conditions of solidification, remelting, and recrystallization, and the experimentally observed structure formation is consistent with this prediction. Conversely, initial solidification in Region B is supposed to occur at the central part of the melt pool. In this case, initial solidification is suggested to occur under lower $G_{cooling}$ and higher $R_{cooling}$ conditions. PF simulations predict the formation of columnar grains, which is consistent with the experimental microstructure. These results demonstrate that the CtFD and PF simulation results can predict the experimental microstructure formation.

4. Conclusion

In the present study, we conducted single-track laser-beam irradiation experiments and corresponding CtFD simulations of Al-Si alloys to obtain guidelines for microstructural control, considering the rapid heating and cooling conditions unique to PBF-type AM processes. Additionally, the microstructures predicted based on the evaluated melting and solidification conditions were compared to the microstructure of the PBFed Al-Si alloy part.

The single-track laser-beam irradiation experiments revealed that the shape of the melt pool changes significantly at a line energy threshold of 0.3 J/mm, and a deeper melt pool is formed under higher line energy irradiation conditions. The CtFD simulations also demonstrate this transition during single-track irradiation. It was found that the transition from thermal conduction-type to keyhole-type melt pool formation occurs at the point where the pre-irradiation heat accumulation temperature exceeds 550 K, and this transition is attributed to the high thermal conductivity.

The CtFD simulations revealed that melting and solidification occurred under rapid heating and cooling rate conditions of $\sim 10^8$ K/s and $\sim 10^7$ K/s, respectively. Fur-

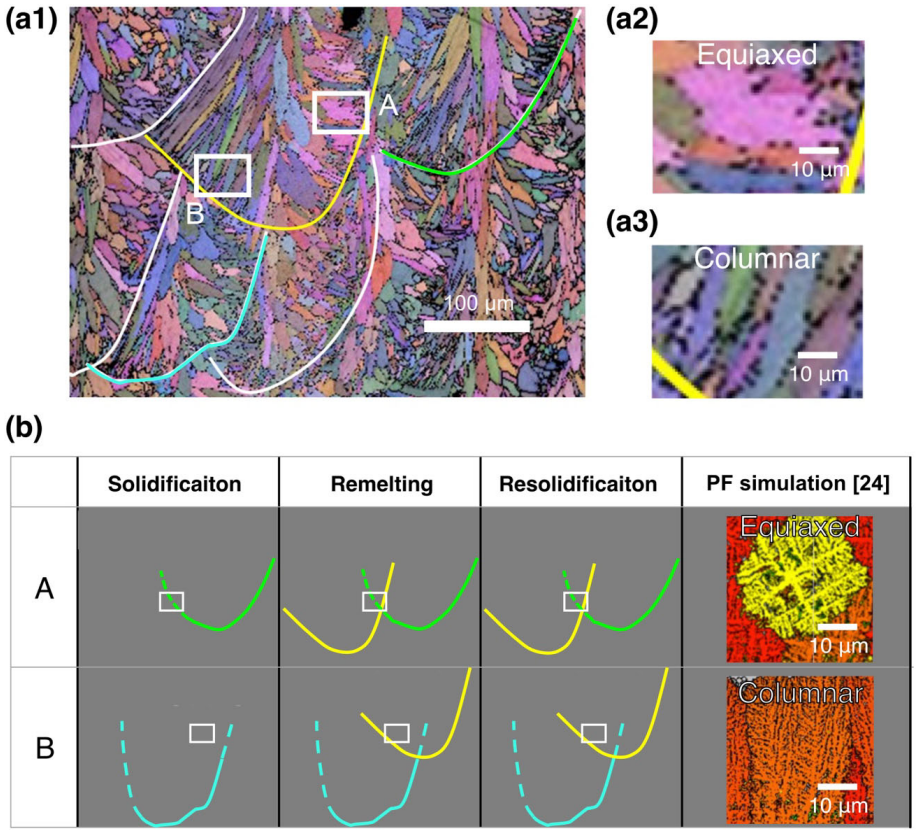

Fig. 7 (a1)–(a3) SEM-EBSD grain maps of laser PBFed Al-10Si part. Grain boundaries are indicated by solid lines. (b) Relative position of regions A and B and microstructure formations predicted by Phase-field (PF) simulations [24]. (online color)

thermore, the melting and solidification conditions vary significantly within the melt pool. The R decreases during melting and increases during solidification. Meanwhile, the G at the solid-liquid interface decreases as both melting and solidification proceed. Thus, the distribution of G in the melt pool region reverses during solidification and melting: melting and solidification occur at the melt pool boundary under conditions of larger G_{cooling} and smaller R_{cooling}, and smaller G_{heating} and smaller R_{heating}. Additionally, a laser irradiation with a larger line-energy condition is suggested to cause a greater difference in the G and R between the interior and boundary of the melt pool. It was indicated that the experimental microstructural inhomogeneity at the melt pool boundary can be explained based on the distribution of melting and solidification conditions within the melt pool.

Acknowledgments

This work was partly supported by JSPS KAKENHI Grant Numbers 21H05193 and 23H01729, by CREST Nanomechanics: Elucidation of macroscale mechanical proper- ties based on understanding nanoscale dynamics for innovative mechanical materials (Grant Number: JPMJCR2194) from the Japan Science and Technology Agency (JST), by the Japan Aluminium Association, by the Japan Institute of Metals and Materials Frontier Grant, by the Amada Foundation, and by the Light Metal Educational Foundation.

REFERENCES

[1] M. Okugawa, S. Kanegae and Y. Koizumi: Multi-axed phase-transforming cellular material: A data-driven design and validation using finite-element method and machine learning, Extreme Mech. Lett. **77** (2025) 102319.

[2] H. Nagayama, S. Kanegae, M. Hosoda, M. Okugawa and Y. Koizumi: Thermally induced phase transforming cellular lattice driven by bimetal beams, MRS Adv. **7** (2022) 701–705.

[3] S. Kanegae, M. Okugawa and Y. Koizumi: Martensitic Phase-Transforming Metamaterial: Concept and Model, Materials **16** (2023) 6854.

[4] A. Suzuki, H. Nakatani, S. Nakagawa, M. Kobashi and Y. Tsuji: Architected materials informatics: Construction and application to cellular-structured heat sink optimization, Acta Mater. **283** (2025) 120557.

[5] J.H. Martin, B.D. Yahata, J.M. Hundley, J.A. Mayer, T.A. Schaedler and T.M. Pollock: 3D printing of high-strength aluminium alloys, Nature **549** (2017) 365–369.

[6] K.V. Yang, Y. Shi, F. Palm, X. Wu and P. Rometsch: Columnar to equiaxed transition in Al-Mg(-Sc)-Zr alloys produced by selective laser melting, Scr. Mater. **145** (2018) 113–117.

[7] A. Aversa, G. Marchese, A. Saboori, E. Bassini, D. Manfredi, S. Biamino, D. Ugues, P. Fino and M. Lombardi: New aluminum alloys specifically designed for laser powder bed fusion: a review, Materials

12 (2019) 1007.
[8] A. Suzuki, T. Miyasaka, N. Takata, M. Kobashi and M. Kato: Control of microstructural characteristics and mechanical properties of AlSi12 alloy by processing conditions of laser powder bed fusion, Addit. Manuf. **48** (2021) 102383.
[9] N. Takata, M. Liu, H. Li, A. Suzuki and M. Kobashi: Fast scanning calorimetry study of Al alloy powder for understanding microstructural development in laser powder bed fusion, Mater. Des. **219** (2022) 110830.
[10] M. Kunieda, A. Suzuki, N. Takata, M. Kato and M. Kobashi: Introducing Hatch Spacing into Deposited Energy Density toward Efficient Optimization of Laser Powder Bed Fusion Process Parameters, Mater. Trans. **64** (2023) 1099–1106.
[11] Y. Otani, N. Takata, A. Suzuki, M. Kobashi and M. Kato: Microstructural origin of anisotropic tensile ductility of Al-Si alloy manufactured by laser powder bed fusion, Scr. Mater. **226** (2023) 115259.
[12] Y. Koizumi and M. Okugawa: Digital Twin Science of Metal Powder Bed Fusion Additive Manufacturing: A Selective Review of Simulations for Integrated Computational Materials Engineering and Science, ISIJ Int. **62** (2022) 2183–2196.
[13] M. Okugawa, K. Saito, H. Yoshima, K. Sawaizumi, S. Nomoto, M. Watanabe, T. Nakano and Y. Koizumi: Solute segregation in a rapidly solidified Hastelloy-X Ni-based superalloy during laser powder bed fusion investigated by phase-field and computational thermal-fluid dynamics simulations, Addit. Manuf. **84** (2024) 104079.
[14] H. Chen, D. Egusa, Z. Li, T. Sasaki, R. Ozasa, T. Ishimoto, M. Okugawa, Y. Koizumi, T. Nakano and E. Abe: Phase-separation induced dislocation-network cellular structures in Ti-Zr-Nb-Mo-Ta high-entropy alloy processed by laser powder bed fusion, Addit. Manuf. **102** (2025) 104737.
[15] T. Ishimoto *et al.*: Superimpositional design of crystallographic textures and macroscopic shapes via metal additive manufacturing—Game-change in component design, Acta Mater. **286** (2025) 120709.
[16] P.V. Cobbinah, S. Matsunaga, Y. Toda, R. Ozasa, M. Okugawa, T. Ishimoto, Y. Liu, Y. Koizumi, P. Wang, T. Nakano and Y. Yamabe-Mitarai: Peculiar microstructural evolution and hardness variation depending on laser powder bed fusion-manufacturing condition in Ti–6Al–2Sn–4Zr–6Mo, Smart Mater. Manuf. **2** (2024) 100050.
[17] Y. Liu, K. Nose, M. Okugawa, Y. Koizumi and T. Nakano: Fabrication and Process Monitoring of 316L Stainless Steel by Laser Powder Bed Fusion with μ-Helix Scanning Strategy and Narrow Scanning Line Intervals, Mater. Trans. **64** (2023) 1135–1142.
[18] M. Okugawa, Y. Isono, Y. Koizumi and T. Nakano: Raking Process for Powder Bed Fusion of Ti–6Al–4V Alloy Powder Analyzed by Discrete Element Method, Mater. Trans. **64** (2023) 37–43.
[19] S. Phoung, E. Williams, G. Gaustad and A. Gupta: Exploring global supply and demand of scandium oxide in 2030, J. Clean. Prod. **401** (2023) 136673.
[20] L. Wang, P. Wang, W.Q. Chen, Q.Q. Wang and H.S. Lu: Environmental impacts of scandium oxide production from rare earths tailings of Bayan Obo Mine, J. Clean. Prod. **270** (2020) 122464.
[21] J. Liu, W. Xiong, A. Behera, S. Thompson and A.C. To: Mean-field polycrystal plasticity modeling with grain size and shape effects for laser additive manufactured FCC metals, Int. J. Solids Struct. **112** (2017) 35–42.
[22] J.D.D. Hunt: Steady state columnar and equiaxed growth of dendrites and eutectic, Mater. Sci. Eng. **65** (1984) 75–83.
[23] M. Okugawa, Y. Ohigashi, Y. Furishiro, Y. Koizumi and T. Nakano: Equiaxed grain formation by intrinsic heterogeneous nucleation via rapid heating and cooling in additive manufacturing of aluminum-silicon hypoeutectic alloy, J. Alloy. Compd. **919** (2022) 165812.
[24] M. Okugawa, Y. Furushiro and Y. Koizumi: Effect of Rapid Heating and Cooling Conditions on Microstructure Formation in Powder Bed Fusion of Al-Si Hypoeutectic Alloy: A Phase-Field Study, Materials **15** (2022) 6092.
[25] P. Ansari and M.U. Salamci: On the selective laser melting based additive manufacturing of AlSi10Mg: The process parameter investigation through multiphysics simulation and experimental validation, J. Alloy. Compd. **890** (2022) 161873.
[26] P.I. O'Toole, M.J. Patel, C. Tang, D. Gunasegaram, A.B. Murphy and I.S. Cole: Multiscale simulation of rapid solidification of an aluminium–silicon alloy under additive manufacturing conditions, Addit. Manuf. **48** (2021) 102353.
[27] P. Wei, Z. Wei, Z. Chen, Y. He and J. Du: Thermal behavior in single track during selective laser melting of AlSi10Mg powder, Appl. Phys. A **123** (2017) 604.
[28] Z. Zhang, T. Zhang, C. Sun, S. Karna and L. Yuan: Understanding Melt Pool Behavior of 316L Stainless Steel in Laser Powder Bed Fusion Additive Manufacturing, Micromachines **15** (2024) 170.
[29] W.F. Templeton, S. Hinnebusch, S. Strayer, A. To and S.P. Narra: Finding the limits of single-track deposition experiments: An experimental study of melt pool characterization in laser powder bed fusion, Mater. Des. **231** (2023) 112069.
[30] M. Okugawa, H. Yoshima, Y. Liu, P. Wang, Y. Koizumi and T. Nakano: Rapid solidification of Hastelloy-X Ni-based superalloy induced by laser-irradiation for powder-bed fusion: applicability and limitation of columnar equiaxed transition criteria, Virtual Phys. Prototyp., submitted.
[31] S.D. Jadhav, L.R. Goossens, Y. Kinds, B. Van Hooreweder and K. Vanmeensel: Laser-based powder bed fusion additive manufacturing of pure copper, Addit. Manuf. **42** (2021) 101990.
[32] Y. Miyata, M. Okugawa, Y. Koizumi and T. Nakano: Inverse Columnar-Equiaxed Transition (CET) in 304 and 316L Stainless Steels Melt by Electron Beam for Additive Manufacturing (AM), Crystals **11** (2021) 856.